

Exoplanet Atmospheres at High Spectral Resolution

Jayne L. Birkby

Abstract The spectrum of an exoplanet reveals the physical, chemical, and biological processes that have shaped its history and govern its future. However, observations of exoplanet spectra are complicated by the overwhelming glare of their host stars. This review chapter focuses on high resolution spectroscopy (HRS) ($R = 25,000 - 100,000$), which helps to disentangle and isolate the exoplanet's spectrum. At high spectral resolution, molecular features are resolved into a dense forest of individual lines in a pattern that is unique for a given molecule. For close-in planets, the spectral lines undergo large Doppler-shifts during the planet's orbit, while the host star and Earth's spectral features remain essentially stationary, enabling a velocity separation of the planet. For slower-moving, wide-orbit planets, HRS, aided by high contrast imaging, instead isolates their spectra using their spatial separation. The lines in the exoplanet spectrum are detected by comparing them with high resolution spectra from atmospheric modelling codes; essentially a form of fingerprinting for exoplanet atmospheres. This measures the planet's orbital velocity, and helps define its true mass and orbital inclination. Consequently, HRS can detect both transiting and non-transiting planets. It also simultaneously characterizes the planet's atmosphere due to its sensitivity to the depth, shape, and position of the planet's spectral lines. These are altered by the planet's atmospheric composition, structure, clouds, and dynamics, including day-to-night winds and its rotation period. This chapter describes the HRS technique in detail, highlighting its successes in exoplanet detection and characterization, and concludes with the future prospects of using HRS to identify biomarkers on nearby rocky worlds, and map features in the atmospheres of giant exoplanets.

Jayne L. Birkby
Assistant Professor
Anton Pannekoek Insitute of Astronomy, University of Amsterdam, Science Park 904, Amsterdam, 1098XH, The Netherlands, e-mail: jbirkby@uva.nl

Introduction

Exploring the exoplanet zoo

It is extremely challenging to directly observe the spectrum of an exoplanet. Not only are exoplanets faint objects, but they are typically located at sub-arcsecond orbital separations, buried in the glare of their host stars that outshine them by factors of a few thousand to billions. However, the spectrum of an exoplanet is the key to understanding the physical, chemical, and biological processes that have shaped its history and govern its future. Therefore, spectroscopic detection is enormously valuable in our quest to understand the striking diversity of the exoplanet zoo (e.g. Fulton et al. 2017; Van Eylen et al. 2017), and in our search for life beyond the Solar system. There are novel ways in which we can infer an exoplanet’s spectrum based on how it affects the total light of the star-planet system throughout its orbit. Although these approaches have delivered the majority of the observed exoplanet spectra to date (see e.g. Sing et al. 2016; Crossfield and Kreidberg 2017), they rely crucially on the planet being favourably aligned so that it passes in front or behind its host star along our line-of-sight, i.e. it forms a transit or secondary eclipse (see Kreidberg’s chapter of this handbook for more discussion on this technique). The chance of this occurring in nature depends predominantly on the stellar radius (R_*) and the orbital separation (a) of the star-planet system: $P_{\text{transit}} \sim R_*/a$. For any planets orbiting the ~ 350 main-sequence stars in our local 10 pc neighbourhood (~ 33 ly; RECONS, Henry et al. 2016, 2018), this chance is typically small (less than 2 percent). Statistical analyses predict that the nearest transiting, potentially habitable, Earth-size planet is located at ~ 11 pc (Dressing and Charbonneau 2015), which makes the seven Earth-size planets orbiting the ultracool dwarf star TRAPPIST-1 at 12.1 ± 0.4 pc particularly interesting (Gillon et al. 2017). However, the nearest *non-transiting*, potentially habitable Earth-size planets, are predicted to be an order of magnitude closer to us, making the non-transiting planetary systems of Proxima Centauri and Ross 128 at just 1.3 pc and 3.4 pc respectively, prime targets in our search for life (Anglada-Escudé et al. 2016; Bonfils et al. 2018). Therefore, in this chapter, we focus on alternative approaches that can disentangle and isolate the light emitted or reflected by the planet itself, regardless of its orbital orientation to our line-of-sight, allowing us to explore the exoplanet zoo and our local neighbourhood in full.

Traditionally, the isolation of planetary light from its host star has been achieved by physically blocking out or nulling the host star using a coronagraph. This has allowed the imaging of widely separated exoplanets ($\text{sep} > 0.1''$, $a > 1$ AU) in broadband filters and more recently spectroscopy at low-to-moderate spectral resolution ($R = \lambda/\Delta\lambda \sim < 4000$; see e.g. Konopacky et al. 2013; Macintosh et al. 2015). Biller & Bonnefoy discuss this in detail in their chapter of this handbook. Here, we will instead investigate how we can use moderate-to-*high-resolution spectroscopy* ($R = 5000 - 100,000$) to study light not only from widely-separated exoplanets, but also those on very close-in orbits ($\text{sep} < 0.005''$, $a < 0.05$ AU). This is important for

our nearest neighbours orbiting the ~ 250 cool M-dwarf stars within 10pc, whose habitable zones are much closer to the host star in comparison to the Sun, with a year lasting on the order of a few tens of days. The techniques we will discuss in this chapter enable not only the spectroscopic detection of the planet and measurement of its true mass, but also a detailed study of its atmospheric properties, including its composition, structure, and its dynamics, including global wind patterns and its rotation period.

Exoplanets at high resolution

Close-in exoplanets: the Doppler Dance

The high-resolution spectroscopy (HRS) technique is rooted in one of the most prolific means of exoplanet detection to date: the Doppler method, also known as the radial velocity technique. In the standard Doppler method, photons from the planet are not detected, thus the planet's existence is inferred. The standard method uses very precise, high-resolution, stable spectrographs to measure the small red- and blue-shift of the host star's spectrum as it moves toward and away from us in response to the gravitational pull of its exoplanet throughout its orbit. The star's radial velocity along our line-of-sight is typically at the 100 meter-per-second (m/s) level for close-in hot Jupiter exoplanets, and approaches the 10 centimeter-per-second (cm/s) level for Earth-like planets orbiting Sun-like stars at ~ 1 AU. The radial velocity semi-amplitude (K_*) of the host star also enables us to determine a lower limit on the planet's mass (M_p) via:

$$K_* = \left(\frac{2\pi G}{P} \right)^{1/3} \frac{M_p \sin i}{(M_p + M_*)^{2/3}} \frac{1}{(1 - e^2)^{1/2}} \quad (1)$$

where P is the planet's orbital period, e is its orbital eccentricity, and i is its orbital inclination, such that $i = 90^\circ$ is edge-on and $i = 0^\circ$ is face-on along our line-of-sight (see Lovis and Fischer 2010 for a full derivation of this equation). It gives only a lower limit on M_p as we cannot assume that we see the full magnitude of the planet's velocity vector, on account of the unknown orbital inclination. The standard Doppler method delivered the first confirmed detection of an exoplanet orbiting a main-sequence host star: 51 Peg b (Mayor and Queloz 1995), which is a non-transiting planet (Henry et al. 1997; Walker et al. 2006; Brogi et al. 2013; Birkby et al. 2017). But it did not give us the spectrum of the planet. To get this, we must instead consider what is happening with the other partner in this Doppler dance i.e. the motion of the planet itself. The gravitational pull of the star imparts a significantly larger orbital velocity to the planet, and so the planet has a radial velocity that is typically orders of magnitude faster than the star, ranging from $K_\oplus \sim 30$ km/s for the Earth-Sun system, up to hundreds of km/s for the closest-in hot Jupiters. Consequently, the red- and blue-shift of the planetary spectral features are much

larger than those of the star, whose stellar spectral features are essentially stationary by comparison. Furthermore, when observing from the ground, any contamination from the Earth's atmosphere, such as telluric water lines, is also essentially stationary. This is illustrated in Figure 1. Therefore, we can use the large wavelength shifts of the planet's spectrum during its orbit to disentangle it from its host star and from our own atmosphere. For this, we must perform high-resolution time-series spectroscopy, observing often enough to sufficiently sample the Doppler shift of the planet, i.e. long enough to detect notable wavelength shifts in the planet's spectrum. The latter is set by the resolution of the spectrograph, with the planet spectrum typically shifting across > 10 pixels of the detector during the time series (see, e.g. Snellen et al. 2010; Birkby et al. 2013).

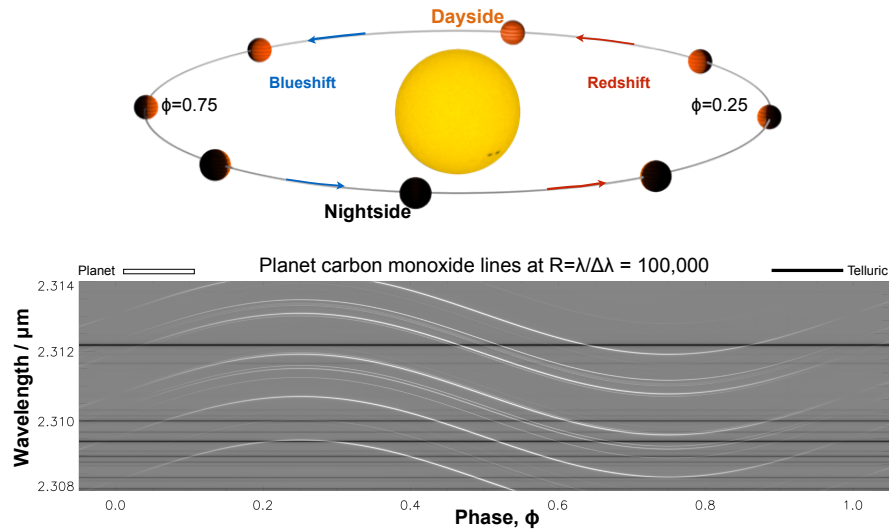


Fig. 1 The high-resolution spectroscopy (HRS) technique. The top panel shows the illumination of a non-transiting planet throughout its orbit, and highlights when its spectrum is red- or blue-shifting. At high-resolution, the planet's spectrum is resolved into a dense forest of individual lines in a pattern that is unique to each molecule (see Figure 2). These lines trace out the radial velocity curve of the planet ($\Delta RV \sim \text{km/s}$), allowing it to be robustly disentangled from the essentially stationary stellar lines ($\Delta RV \sim \text{m/s}$) and the contaminating spectral lines from Earth's telluric features. The maximum rate of change of velocity is reached around superior and inferior conjunction. At the quadrature points highlighted in the top panel, the spectral lines of the close-in planet are maximally separated in velocity from the host star and tellurics, but the change in the Doppler shift of the planet lines is small here making it difficult to disentangle them from the tellurics. The planet can be observed via its thermally emitted spectrum, or by the spectrum it reflects from the host star. Star-planet image ©Ernst de Mooij.

The concept of using high-resolution spectroscopy to study exoplanet atmospheres in this way arose not long after the discovery of 51 Peg b. For example, the high-resolution ($R = 100,000$) infrared spectrograph CRIRES at ESO's Very Large Telescope (VLT) was designed with this purpose in mind (Wiedemann 1996,

2000), aimed at detecting the direct thermal emission spectra of exoplanets. Others searched instead for the reflected light from the hot Jupiter τ Boo b with optical high-resolution spectrographs (Charbonneau et al. 1998, 1999; Collier Cameron et al. 1999; Collier-Cameron et al. 2004), although only found upper limits. Many of the diagnostic properties of high-resolution spectra of exoplanets were outlined by Brown (2001) and Sparks and Ford (2002), and multiple attempts were made to detect thermally emitted light from giant exoplanets at infrared wavelengths. These included using high-resolution spectrographs such as NIRSPEC on Keck II and Phoenix on Gemini South (e.g. Brown et al. 2002; Deming et al. 2005; Barnes et al. 2007b,a) but again only provided upper limits. It was only when Snellen et al. (2010) used CRILES to observe the hot Jupiter HD 209458 b that the technique delivered its first robust detection of a molecule (carbon monoxide) in an exoplanet atmosphere. Although poor weather may have inhibited earlier attempts with other instruments, the stability of CRILES, in part delivered by its use of adaptive optics (to keep maximal flux of the star centred on the slit entrance of the spectrograph) and Nasmyth mounting (to stop the instrument moving around), and its superior spectral resolution, were undoubtedly instrumental to its success. Since then, high-resolution spectroscopy has been used to study the atmospheric composition of both transiting and non-transiting close-in giant planets (Brogi et al. 2012; Rodler et al. 2012; Birkby et al. 2013; de Kok et al. 2013; Rodler et al. 2013; Brogi et al. 2013; Lockwood et al. 2014; Brogi et al. 2014; Schwarz et al. 2015; Hoeijmakers et al. 2015; Brogi et al. 2016; Piskorz et al. 2016; Birkby et al. 2017; Allart et al. 2017; Brogi et al. 2017; Piskorz et al. 2017; Nugroho et al. 2017; Brogi et al. 2018), and has provided some upper limits on mini-Neptune and super-Earth atmospheres (Crossfield et al. 2011; Esteves et al. 2017). Note that while the majority of these studies focused on detecting the dayside thermal emission of the planet, several of them also observe the planet during its transit, thus highlighting that traditional transmission spectroscopy is also possible with HRS.

Although we can use the Doppler shift to our advantage, there remains the significant challenge of the planet-to-star flux contrast ratio, which ranges from 10^{-3} to 10^{-10} for hot Jupiters to Earth-Sun analogues, respectively, with the planet spectrum buried in the noise of the stellar spectrum. This is where the increased spectral resolution aspect of the HRS technique becomes crucial. Each spectral line of the planet spectrum is detectable to a certain significance, and the deeper the line, the easier it is to detect. The more lines we can include in our measurement, the higher the significance of our detection. At low spectral resolution, spectral lines are convolved to shallower depths due to the limited resolving power of the instrument, and also blended with other nearby lines. Figure 2 demonstrates this effect. The overplotted points in the figure represent the typical resolution currently achieved with observations of exoplanets from e.g. the Hubble Space Telescope (Kreidberg et al. 2014b), while the highest resolution ($R=100,000$) represents ground-based spectrographs, such as CRILES. Space-based spectrographs are typically lower in resolution because the increased volume, and hence weight of the instrument at higher spectral resolution makes them too expensive and cumbersome to launch. At high spectral resolution we better retain both the depth and plurality of the spectral

lines. By detecting multiple spectral lines, we boost the signal-to-noise of the planet by the square root of the number of lines we detect ($\sqrt{N_{lines}}$). This makes high-resolution spectrographs with *wide instantaneous spectral coverage* (i.e. number of wavelengths observed in a single exposure) highly suited to the technique. Figure 2 also highlights the very specific and *unique* pattern of lines that each molecule produces (water and carbon monoxide in a hot Jupiter are shown as an example). These patterns are difficult to mimic by chance at high spectral resolution, adding confidence to the detection of the molecule. At lower resolution, great care must be taken to accurately separate the blended, broad molecular bands of different molecules, and to precisely remove any systematic effects that can introduce mimics that are orders of magnitude larger than the planet signal. Kreidberg’s chapter of this handbook explains the removal of systematics from lower-resolution spectra in detail.

Let us assess the signal-to-noise we can expect to achieve for a planet using the HRS technique. For a close-in exoplanet, assuming that we can completely remove the contaminating effects of the Earth’s atmosphere, we can write to first order the signal-to-noise ratio of the planet spectrum obtained via HRS as follows (Snellen et al. 2015):

$$\text{SNR}_{\text{planet}} = \frac{S_p \sqrt{N_{lines}}}{\sqrt{S_* + \sigma_{bg}^2 + \sigma_{read}^2 + \sigma_{dark}^2}} \quad (2)$$

where S_p and S_* are the signal from the planet and star respectively, both in units of photons per resolution element. σ_{bg} , σ_{read} , and σ_{dark} , represent noise from the sky and telescope background, the read-out noise, and the dark current from the detector, respectively. N_{lines} is the number of lines *detected* in the observed wavelength range, i.e. it accounts for both the *plurality* and *strength* of the lines in the planet spectrum, and is thus dependent on the spectral resolution. In the photon-limited regime, this reduces to the equation below:

$$\text{SNR}_{\text{planet}} = \left(\frac{S_p}{S_*} \right) \text{SNR}_{\text{star}} \sqrt{N_{lines}} \quad (3)$$

where $\left(\frac{S_p}{S_*} \right)$ is the planet-to-star signal ratio (e.g. the planet-star flux ratio or the amplitude of the expected transmission signal) and $\text{SNR}_{\text{star}} = \sqrt{S_*}$ is the photon-limited, *total* signal-to-noise of the host star. For example, assuming blackbody radiation, let’s take a hot Jupiter and host star with a dayside flux contrast ratio of 5×10^{-4} . Let’s also assume our spectrograph throughput enables a signal-to-noise ratio on the star of 200 in 3 minute exposure, and that we observe continuously for a half night (~ 5 h, ~ 100 exposures), targeting the CO molecule. Let’s also assume our spectrograph has sufficient resolution to resolve 30 lines in the $2.3 \mu\text{m}$ CO ro-vibrational overtone. The total $\text{SNR}_{\text{star}} \sim 2000$ results in $\text{SNR}_p = 5 \times 10^{-4} * 200 * \sqrt{100} * \sqrt{30} \sim 5.5$. This assumes that all the detected CO lines are equally and maximally deep.

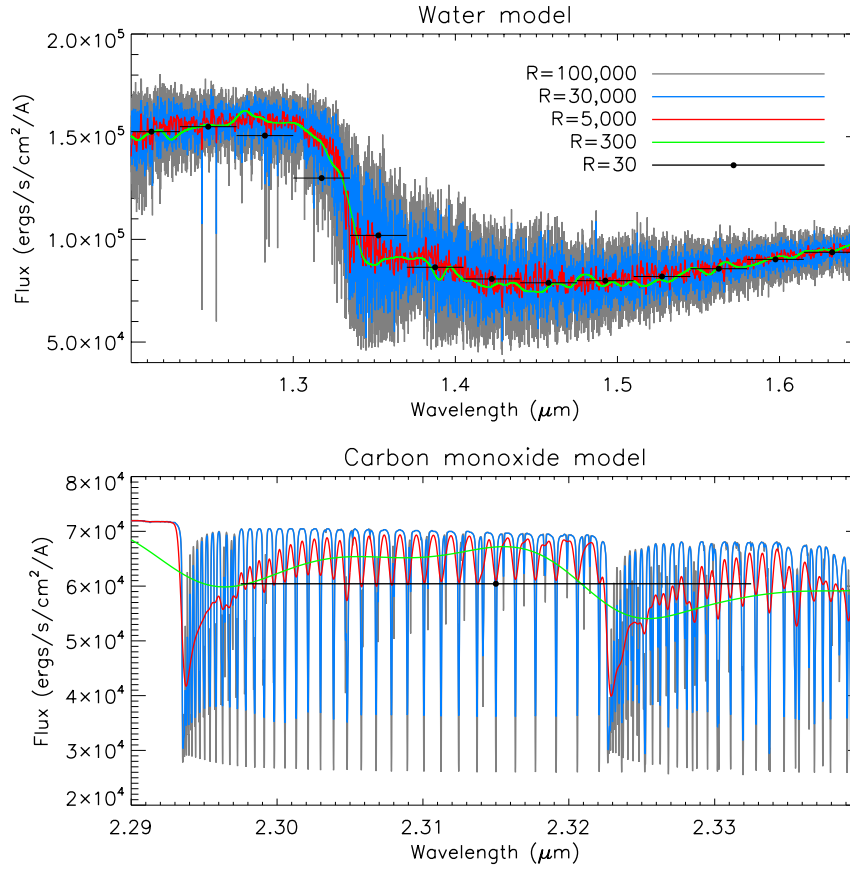


Fig. 2 The effect of decreasing spectral resolution. The two panels show different wavelength regions of a model hot Jupiter atmosphere containing water and carbon monoxide. Note the difference in the x-axis scale. The model has been convolved to different spectral resolutions. The overplotted points represent the typical resolution resulting from current space-based observations and trace out only broad molecular features. Note how many individual CO lines are lost between a resolution of $R=100,000$ and $R=300$. The shallower lines disappear more quickly, but some of the stronger CO lines remain even at $R=5,000$, albeit much reduced in line depth. Each line that is detected with the high-resolution technique increases the total planet signal-to-noise by a factor of $\sqrt{N_{lines}}$.

Seeing through the Earth's atmosphere

To detect the planet's spectral lines, we must first remove the contaminating telluric lines present in ground-based observations, taking advantage of the fact they do not vary in wavelength over the time span of the observations, unlike the planet. Before beginning this step, it can be beneficial to perform the following procedures. First, clean any remaining bad pixels from the extracted spectra, then align them to a

common wavelength grid. The alignment removes drift caused by e.g. changes in the temperature of the instrument or telescope (e.g. Brogi et al. 2013). To preserve the behaviour of any systematic effects in the observations, it is also more suitable to work with the spectra in their observed pixel spacing rather than re-linearize them to regular wavelength grid. It is also therefore advantageous to have a highly stable spectrograph and consistent observing strategy that negates significant realignment of the spectra, even at the sub-pixel level.

Finally, it can be very useful in the beginning to inject a model planet spectrum into the data at an appropriate orbital velocity, to act as a guide during the telluric removal process (see panel E of Figure 3). The injected model should reasonably match the expected atmospheric profile and composition, and should be only just detectable so not to significantly alter the noise properties of the data. This enables a check on when the telluric removal process begins to also remove planet signal, and highlights if the telluric cleaning process is altering the planet spectral lines. It also enables a means to assign weighting over the spectral range of the dataset to account for, e.g. noisy detectors that naturally give lower signal strength in the template-matching process. If the model is poorly recovered in a spectral order, then the real planet signal will likely also have lower detectability in this range and can be down-weighted for the template matching. Of course, the injected signal should be removed in the final analysis of the spectra.

Standard techniques to remove telluric lines typically use an observed telluric standard A-star before or after each science spectrum to correct the data (e.g. Crossfield et al. 2011). However, because we want to observe the planet lines Doppler shifting and gain as much signal-to-noise as possible, we cannot continuously interrupt the observation to take telluric standards. Sparsely observed telluric standards are not a good representation of the atmosphere during the spectral time series, and can therefore leave significant residuals. Since the telluric lines only change in depth and not position over time, an alternative approach is to simply model the flux observed in each pixel of the spectrum over the time series. The main cause of the variation in the telluric lines is usually changes in air mass, followed by changes in e.g. telescope temperature, in-slit position, and seeing. After normalizing the spectra, we can use linear regression to form a function that describes the behaviour of the tellurics in each pixel of the spectrum over time and remove them (this is a column-by-column operation on the matrices shown in Figure 3). The final step is to divide each column by its variance to restore the noise properties of the renormalized data, and stop very noisy residual pixels from dominating. Any remaining large scale, low-order gradients can be removed with a high-pass filter applied to each spectrum. This has proven effective in multiple planet detections (e.g. Snellen et al. 2010; Brogi et al. 2012, 2013, 2014, 2017, 2018). In some cases however, additional unknown systematics persist. In these cases, we can instead adopt a blind approach to modelling the telluric variations in each pixel over time. Singular value decomposition (SVD; Kalman 1996), or principle component analysis (PCA; Murtagh and Heck 1987; Press et al. 1992), can be used to find common modes over time for each pixel in the spectral time series. The idea here is that the Doppler-shift of the planet moves its spectrum across the pixels during the time series; thus it is not identified as

a common mode for any one particular pixel. The procedure removes the tellurics and stellar continuum, leaving behind the continuum-normalized planet spectrum buried in the residual photon noise. A demonstration of the different stages of telluric removal with the PCA method is shown in Figure 3. Various implementations of this approach have made multiple successful planet detections (e.g. de Kok et al. 2013; Birkby et al. 2013; Piskorz et al. 2016; Birkby et al. 2017; Piskorz et al. 2017), including algorithms that enable weighting of the data by their errors, such as the popular SYSREM algorithm typically applied transit survey light curves (Tamuz et al. 2005). However, in all of these approaches, the spectra are normalized, which removes information about the true continuum level of the planet. The removal of the continuum means that models with different abundances and atmospheric temperature profiles can look very similar, especially when comparing the depths of different lines in the spectrum, and thus introduces degeneracies. An alternative approach to remove the telluric features is to model them using theoretical calculations based on the atmospheric conditions during the exposure, using codes such as ESO’s MOLECFIT or TERRASPEC (e.g. Rodler et al. 2012; Lockwood et al. 2014; Smette et al. 2015). Modelling the tellurics directly has the advantage of preserving the continuum of the planet spectrum. On the other hand, it does not automatically account for additional instrumental systematic effects occurring during the observation, again leaving residuals. The best approach to telluric removal is still under refinement, although the different approaches can already produce residual spectra with noise approaching their theoretical photon limit within 5 – 20% (Brogi et al. 2014). Only in the cores of the deepest telluric lines does the noise still significantly exceed the photon limit (by a factor of a few), but since these represent a small fraction of the data, the analysis of HRS data overall approaches the theoretical photon limit, which conversely is seldom achieved at lower spectral resolution.

In some cases, at certain wavelengths, the star may also contain sufficiently similar spectral lines to the planet (e.g. CO lines at $2.3\mu\text{m}$ in hot Jupiters and cooler host stars such as K-dwarfs), or may undergo non-negligible velocity changes (e.g. high mass ratio systems such as a hot Jupiter orbiting a cool small M-dwarf), such that it can interfere with the telluric removal process. The stellar lines can be modelled and removed before tackling the tellurics. Brogi et al. (2016) and Schwarz et al. (2016) describe iterative approaches to this with a model atmosphere that can also include astrophysical alterations to the line profile, e.g. the Rossiter-McLaughlin effect during the transit of the planet.

Finding the planet in the noise

With the telluric and stellar lines removed from the spectra, we are left simply with the residuals, as shown in the lower panels of Figure 3, which contain noise and the planet’s spectral lines. The individual planet lines have low signal-to-noise ($\text{SNR}_{\text{line}} \sim < 1$), so we must combine their signals to detect the planet spectrum (as indicated in Equation 3). A powerful approach to this is the cross-correlation method, which uses a template spectrum appropriate for the planet atmosphere to

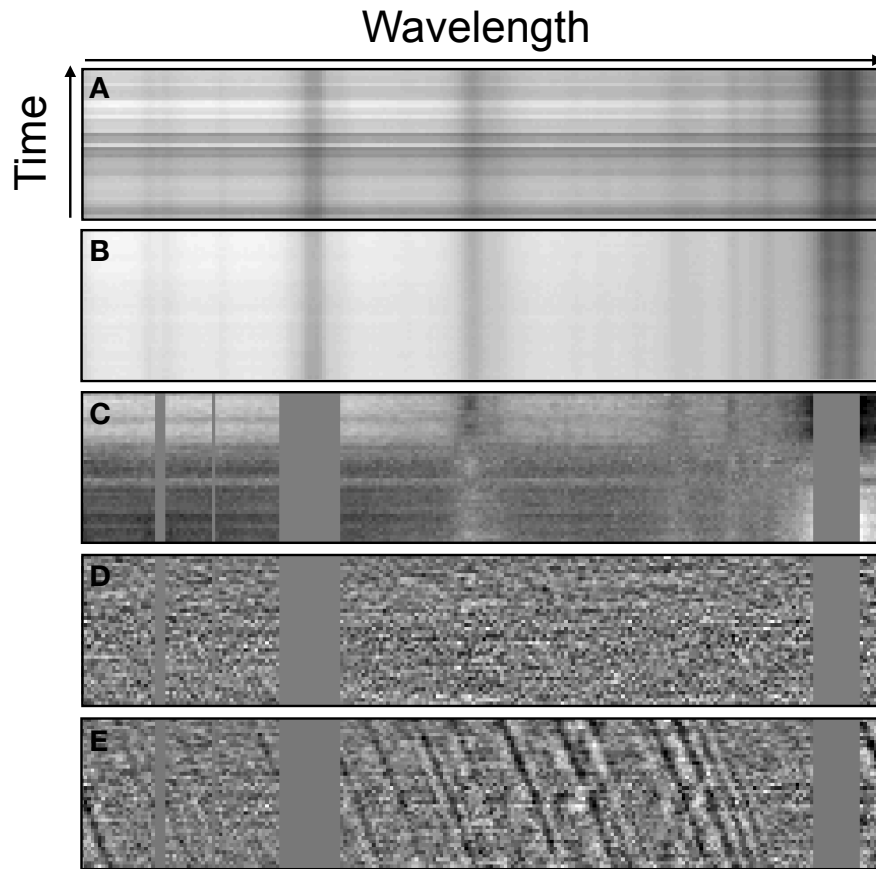


Fig. 3 Stages of the telluric removal process using principle component analysis. These data are from Birkby et al. (2017) who observed the dayside of 51 Peg b at $3.2\mu\text{m}$ for 5 hours with CRIRES/VLT. There are 42 spectra in the time series. **A)** The observed spectra extracted from the CRIRES pipeline, after residual bad pixel cleaning and alignment to a common wavelength grid. **B)** The normalized spectra. **C)** After removing the first principle component. **D)** After removing optimal components, determined as when the planet signal starts to also be removed. The individual spectral lines of the planet are buried in the residual noise. **E)** The same as D but with a model water spectrum injected at stage A at $100\times$ the nominal planet single strength to highlight the positions of the planet's spectral lines. Solid gray regions are saturated telluric or stellar lines that have been masked. Note the gradual removal of the telluric feature in the center of each panel. The individual lines of the planet are blue-shifting as it moves toward us after superior conjunction, as shown by the slanted features in panel E, which trace out a small portion of the planet's RV curve.

scan through the residuals of each observation and compare how well the template matches the specific line positions, and the ratio of the line depths, in the observed planet spectrum. It is a fingerprint matching exercise for exoplanet atmospheres.

The templates should match the spectral resolution and velocity resolution of the data, and are generated by a comprehensive radiative transfer treatment that models the interaction of light with the matter in the atmosphere. Heng’s chapter of this handbook introduces this, and is elaborated in, e.g. Heng (2016). The depth of the lines and their relative depth ratios in the template spectra are governed largely by the composition of the model atmosphere and its temperature-pressure ($T - P$) profile. The latter describes how the temperature changes in the atmosphere as a function of pressure (or altitude). On Earth, the $T - P$ profile is partially inverted creating a stratosphere i.e. there is a layer that heats up after an initial cool-off with increasing altitude. It is caused by ozone absorbing UV radiation and heating the atmosphere. $T - P$ inversions result in emission lines, rather than absorption lines in the spectrum. A weak inversion may only fill in the cores of the absorption lines, leaving an apparently shallower feature suggesting an isothermal structure instead (e.g. Schwarz et al. 2016; Parmentier et al. 2018). The higher the spectral resolution, the easier it is to identify these more complicated line shapes in the spectrum of the exoplanet.

Another crucial input to creating the template spectra is a precise list of line positions and opacities for different molecules at different temperatures and pressures. These are either measured in the laboratory, or (in cases where it is not possible to do this safely) with ab initio calculations from quantum chemistry. There are several databases that provide such line lists and opacities, including HITRAN and HITEMP (Rothman et al. 2013; Gordon et al. 2017; Rothman et al. 2010), and ExoMol (Tennyson et al. 2016). At low spectral resolution, inaccuracies in the individual line positions are more tolerable as they are blended and convolved by the instrument, as shown in Figure 2. However, at high resolution accurate line positions become crucial. Even if we have used the correct properties for the planet atmosphere, the cross-correlation will not get a good match if the theoretical or laboratory-measured values of the line position are incorrect. We will have lost our $\sqrt{N_{lines}}$ advantage. For simple molecules, e.g. CO, the line positions are very well determined. However, for more complex molecules such as water (H_2O) and methane (CH_4), there remain some inaccuracies in the line positions at high spectral resolution at temperatures appropriate for hot Jupiters, as demonstrated in Hargreaves et al. (2015). It highlights the importance of laboratory research in the pursuit of understanding the full diversity of the exoplanet zoo (e.g. Hörst et al. 2018).

Once we have generated a suite of templates that could plausibly match the planet’s observed spectrum, we can use them to perform cross-correlations to find the planet signal. Each cross-correlation gives a detection strength (i.e. how well the template matches the data) for each trial wavelength shift (or velocity shift). The step size between trial shifts should be no smaller than the velocity resolution of the pixels on the detector to avoid oversampling the data. Figure 4 highlights how the peak of each cross-correlation function (CCF) moves in response to the Doppler shift of the planet, tracing out part of its radial velocity curve from which we can

determine the radial velocity semi-amplitude of the planet, K_p . For transiting planets, we already know this velocity because $\sin i$ is solved. For non-transiting planets, we must find K_p by determining the slope of the CCF trail. To do this, we can shift the CCFs into the rest frame of the planet, assuming a given K_p . The total Doppler shift of the planet not only includes its radial velocity (V_{RV} , which can account for eccentric orbits), but also the center-of-mass velocity of the star-planet system with respect to the Earth (V_{sys}). This is typically measured using the standard Doppler method on the host star. Finally, we must include the velocity of the observer i.e. the velocity induced by the motion of the Earth around the Sun (the barycentric correction, V_{bary}). We can write the total planet velocity (V_p) as:

$$V_p = V_{RV} + V_{sys} + V_{bary} \quad (4)$$

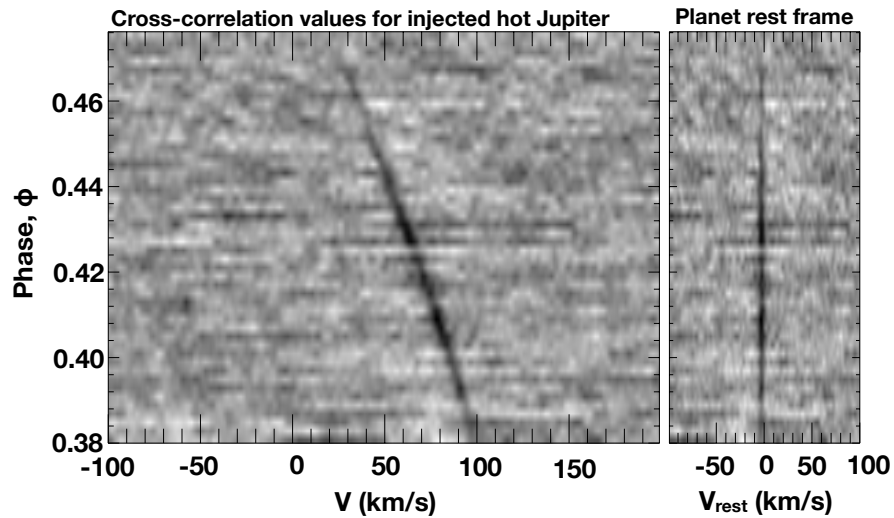


Fig. 4 Left: Part of the radial velocity curve observed over 5 hours for an injected model hot Jupiter. The RV trail is traced out by the blue-shifting peak of the cross-correlation functions (CCFs). The model contains water lines and was injected into real observations of HD 189733 from Birkby et al. (2013) at $5\times$ the nominal model strength for clarity. The slope of the trail corresponds to the RV semi-amplitude of the planet, K_p . Right: The CCFs shifted into the planet rest frame, where $K_p = 154$ km/s. The aligned CCFs can be summed into a single CCF for each trial K_p , which creates each row in Figure 5.

Once in the planet rest frame, we can sum the CCFs, combining signal from all of the lines in all of the observed spectra. If we repeat this process for a range of different K_p , we find which K_p gives the strongest peak in the summed CCF. This is shown in Figure 5. As we approach the true K_p of the planet and the CCF peaks align, we see a stronger peak in the summed CCF. Importantly, this peak should occur at zero velocity in the planet rest frame as it confirms that the signal is at the same V_{sys} as the host star. Significant deviations from V_{sys} generally indicate that

the signal is not planetary in nature. However, in some cases, physical phenomena occurring in the planet’s atmosphere, such as strong day-to-night winds and heat circulation can cause offsets of a few km/s (e.g. Snellen et al. 2010; Miller-Ricci Kempton and Rauscher 2012; Showman et al. 2013; Brogi et al. 2016; Zhang et al. 2017). This is discussed further below.

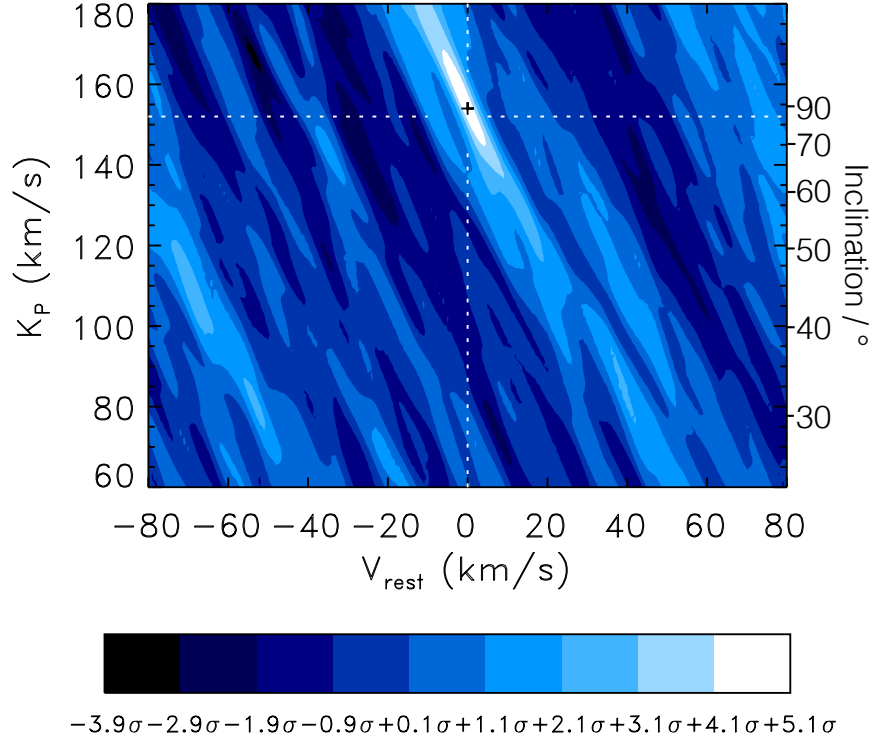


Fig. 5 A 5σ detection of water in the hot Jupiter HD 189733 b using the high-resolution spectroscopy technique. Each row in the matrix is a summed cross-correlation function for a given planet RV semi-amplitude (K_p). When the correct K_p value is approached, the individual peaks of the CCFs align and contribute maximally to the signal. The white contour represents the 1σ error ellipse in K_p and V_{sys} , and is coincident with the rest frame velocity of the planet (dotted lines). This velocity includes the center-of-mass velocity of the star-planet system, and helps confirm the planetary nature of the signal. Note that there are regions corresponding to 3σ significances, highlighting the importance of exploring the parameter space around the expected V_{sys} and K_p of the planet, even in transiting cases. The planet mass and its orbital inclination can be derived given the value of K_p , as shown in Equations 5 and 6. The derived inclinations for given K_p values are shown on the right-hand y-axis.

The final step in securing the exoplanet’s spectroscopic detection is to determine the significance level of the signal. The distribution of the cross-correlation values is Gaussian (see, e.g. Brogi et al. 2012), so we can make a simple approximation of the significance of the planet signal by dividing the CCFs by their standard deviation.

A more robust approach is to compare the CCF values in the radial velocity trail of the planet to those outside it, and use a Welch T-test (Welch 1947) to determine the probability that both populations are drawn from the same parent distribution. This can be done at each trial K_p . Figure 5 shows the distribution of these probabilities. Values of $\leq 3\sigma$ can be seen throughout the parameter space and are false positives, or aliases generated by the autocorrelation function of the template. It is therefore important to explore the region around the expected planet rest frame velocity and expected K_p to determine the errors on the measured quantities. We could go back to the residual spectra and align and sum them into the planet rest frame using the measured K_p to create an actual spectrum of the planet. However, given that each line has very low signal-to-noise, the spectral features are difficult to discern. For example, for a planet detected at 6σ using 50 spectra with each containing 30 strong CO lines, then the individual lines in the summed spectrum would be expected to be present at a significance of $\sim 1.1\sigma$ and at $< 0.2\sigma$ per spectrum. However, in some cases, it is possible to see the strongest lines of, e.g. carbon monoxide, extending clearly from the noise (see, e.g. Brogi et al. 2012; Schwarz et al. 2016).

An alternative approach to detecting the planet spectrum is to leave the stellar spectrum intact and treat the system in a similar way as stellar binaries, using techniques such as Todcor (Zucker and Mazeh 1994). This performs a cross-correlation with two templates simultaneously, one for the star and one for the planet. It works optimally when the lines of the planet and stellar spectra are maximally separated (i.e. at quadrature), unlike the previously described method which works best when the planet is undergoing its greatest rate of velocity change (i.e. before and after superior/inferior conjunction, but avoiding exact conjunction times due to the star and planet spectral lines overlapping). Todcor yields a two-dimensional array of CCFs for each component of the system per spectrum. These can be combined into nightly stellar and planetary likelihood curves in which to search for peaks caused by the planet at V_{sys} (see examples in Lockwood et al. 2014; Piskorz et al. 2016, 2017). This approach can be more beneficial in systems that undergo less velocity change e.g. giant planets on longer orbital periods, and helps probe the exoplanet population that move too slowly for HRS, but are still too close to their host star to isolate, even with the assistance of high-contrast imaging (as described further below).

Model-independent planet masses and radii

The measurement of K_p converts the star-planet system into a double-lined spectroscopic binary. We can therefore derive the true mass of non-transiting planets, despite not knowing the orbital inclination, via the velocity and mass ratios:

$$\frac{K_\star}{K_p} = \frac{M_p}{M_\star} \quad (5)$$

where M_\star is determined from stellar evolution models. We can then even derive the planet's orbital inclination in non-transiting systems, via:

$$\sin i = K_p / V_{orb} \quad (6)$$

assuming a circular orbit, where $V_{orb} = 2\pi a / P$, and that the mass of the planet is negligible compared to the host star mass. The typical precision in the derived planet mass is at the 5% level (de Kok et al. 2013) and acts as proof of the planetary mass nature of non-transiting systems; a particularly important aspect for our nearest rocky neighbours. If the planet is also a transiting system, HRS converts it to a double-lined eclipsing binary system, allowing model-independent measurements of the mass and radius of the host star and its planet. Such systems are important calibrators for stellar evolution models, especially for M-dwarfs, the most common stars in our local neighbourhood. Stellar models tend to underpredict the radii of small stars by $\sim 3 - 15\%$ (see e.g. López-Morales and Ribas 2005; Torres et al. 2010; Irwin et al. 2011; Birkby et al. 2012; Baraffe et al. 2015; Dittmann et al. 2017; Lubin et al. 2017; Jackson et al. 2018; Kesseli et al. 2018), which can lead to a miscalculation of the planet’s radius and thus its atmospheric properties.

Widely-separated exoplanets

Exoplanets on wide orbital paths move slowly. This means their spectral features do not change their Doppler shift significantly during the course of a nightly observation, and thus require a different approach to isolating their spectra from the glare of their host stars and Earth’s telluric features. Traditional high-contrast imaging (HCI) techniques suppress a fraction of the light of the star at the planet’s position, thus improving the star-planet contrast ratio. An example of this is adaptive optics (AO), which corrects for the turbulence in the Earth’s atmosphere and aims to deliver diffraction-limited images. This not only creates a very sharp image of the star and a better spatial resolution of the star and planet but also adds stability to the observations, ensuring that the star does not wander around on the detector (or in the entrance of a spectrograph). We saw in the previous sections that high-resolution spectroscopy further enables us to increase the signal-to-noise of the planet by combining many of its spectral lines via cross-correlation. The combination of these two techniques (HRS+HCI) is a powerful tool for exoplanet spectroscopic detection and characterization, and is described in detail by Sparks and Ford (2002) and Snellen et al. (2015). In the case of HRS+HCI, the Doppler-shift advantage is replaced by the fact that the planet’s spectrum is uniquely different to the star and *strongly localized*. In a simple long-slit spectrograph, the star fills most of the slit and its light is detectable over many rows on the detector, while the fainter planet spectrum is typically only detectable in one row. This requires the entrance slit of the spectrograph to be aligned to contain both the star and the planet. In an integral field unit (IFU), every “pixel” (or spaxel) is effectively an entrance to the spectrograph and thus generates its own spectrum. We can therefore use rows or spaxels containing only the stellar spectrum and tellurics as a template that can be scaled and removed

from every row or spaxel, leaving behind only the planet spectrum at its unique location, buried in the residual noise. The planet is then detected by cross-correlating the residuals in each row or spaxel with a model template, with the strongest peak in the CCFs occurring at the planet’s position. Note that the planet’s spectrum will still contain its radial velocity at the time of observation, providing a data point on the planet’s long-period RV curve, which helps determine its orbit in combination with astrometry from direct images (e.g. Schwarz et al. 2016).

We can rewrite the equation for the expected signal-to-noise of the planet using HRS+HCI as follows:

$$\text{SNR}_{\text{planet}} = \left(\frac{S_p}{S_\star} \right) \text{SNR}_{\text{star}} \sqrt{c_{\text{HCI}} N_{\text{lines}}} \quad (7)$$

where c_{HCI} is the suppression factor of the stellar flux at the planet position. It is important to note that if c_{HCI} is too strong, we fall out of the photon-limited noise regime and into the sky background-limited regime. Beyond $5\mu\text{m}$, sky background begins to dominate; hence, in cases of strong c_{HCI} traditional direct imaging processing techniques may be more sensitive than HRS+HCI. The first successful demonstration of HRS+HCI was achieved by Snellen et al. (2014), who observed the young giant exoplanet β Pic with CRIRES/VLT. The planet was detected at its known spatial location by matching with a model atmosphere spectrum containing carbon monoxide, and its measured RV showed a blue-shift that helped determine the likelihood of it transiting its host star in 2017-2018. The planetary mass companion GQ Lup b was also detected using this technique, appearing at its known location matching with carbon monoxide and water model atmosphere spectra, at a signal-to-noise of $\text{SNR}_p \sim 12$ and clear CO absorption lines in the extracted planet spectrum (Schwarz et al. 2016). Even at $R = 4000$, cross-correlation can still detect the presence of CO and water in the atmospheres of widely separated planets (Barman et al. 2015). Hoeijmakers et al. (2018) further demonstrate the enormous potential of using moderate-resolution IFUs to create “molecule maps” which locate the position of the planet and detect its atmosphere by combining HRS+HCI, opening new avenues for direct imaging survey strategies.

Atmospheric properties

The use of model atmospheric spectra in the high resolution spectroscopy technique means that it not only detects the planet, but simultaneously characterizes its atmosphere. By using model atmospheres (rather than a binary mask), the technique goes beyond revealing the mere presence of a molecule, and places constraints on the chemical abundances in the atmosphere, as well as the temperature-pressure profile. The more lines and molecules that HRS can detect, the stronger its constraint on the planet’s atmospheric composition. To determine some the planet’s atmospheric properties in the cross-correlation analysis, it can be helpful to inject the best-matching model into the observed spectra (at the planet velocity) with dif-

ferent negative scaling factors, and re-run the full analysis starting at the telluric removal. When the planet signal is completely canceled (a 0σ detection), the line contrast can be measured i.e. the depth of the deepest planet lines with respect to the continuum, divided by the stellar flux. This line contrast, which is convolved by the resolution of the spectrograph, indicates the difference between the line cores in the planet spectrum and its broadband continuum, and thus helps constrain the T-P profile and abundances in the planet atmosphere. Multiple models from the grid of T-P profiles and abundances tried in the cross-correlation could provide matches within 1σ of the best-matching model, and thus provide an estimate of the errors on these properties. de Kok et al. (2013) highlighted pathways to achieve tight constraints on abundances with HRS alone, proposing spectrographs with a wide instantaneous spectral coverage as key instruments for its success. They also note that an additional advantage of high-resolution spectroscopy is its ability to probe above cloud decks where the cores of the strongest spectral lines are formed. Lower-resolution spectra see only muted spectral lines; thus, HRS potentially enables measurements of the composition of cloudy worlds that have eluded lower-resolution observations (see, e.g. Kreidberg et al. 2014a).

A multi-resolution approach

de Kok et al. (2014) highlight the power of combining both low-resolution spectroscopy (LRS) and HRS measurements, which can tightly constrain the $T - P$ profile and continuum level of the planet, thus removing degeneracies with composition. Brogi et al. (2017) demonstrated this using multi-resolution spectra of HD 209458 b, determining the planet's metallicity to $0.1 - 1 \times$ its host star value. Pino et al. (2018) also demonstrated the effectiveness of multi-resolution spectra by confirming that the flat spectrum of HD 189733 b (likely due to scattering from aerosols) seen at low resolution can be reconciled with the sodium spectral feature seen at high resolution. Multi-resolution spectroscopic observations are therefore highly valuable in characterizing exoplanet atmospheres, and hence in understanding their formation history and evolution.

Spinning worlds

A unique aspect of HRS is that it is sensitive to the precise shape of the lines in the planet spectrum. For a rotating planet passing through transit, the leading limb of the atmosphere is red-shifting while the trailing limb is blue-shifting. However, the disk-integrated observation of current HRS merges these into a single broadened spectral line that results in a CCF for the planet that is broader than expected from the model and instrument resolving power. This effect was seen the case of the widely separated giant exoplanet β Pic b, resulting in the first measurement of the length of a day on an exoplanet. Its rotational velocity along our line-of-sight was $V_{rot} \sim 25$ km/s, corresponding to a day length of ~ 8 hours (Snellen et al. 2014). This

is faster than Jupiter's ~ 10 hour day, and the young exoplanet is expected to further spin up as it cools and contracts. GQ Lup b on the other hand only rotates at ~ 5 km/s, which may be due to its young age (Schwarz et al. 2016). Understanding how planets spin and acquire their angular momentum is a key part of their formation history. Planets that have migrated to very close-in orbits are expected to be tidally locked to their host star. Brogi et al. (2016) measured the rotational period of the hot Jupiter HD 189733 b to be $P_{rot} = 1.7_{0.4}^{+2.9}$ days, which is consistent within the errors with the orbital period of ~ 2.2 days and significantly slower than observed for younger exoplanets that are not tidally locked.

Windswept worlds

Another advantage of direct spectroscopic detection with HRS is its sensitivity to small velocity shifts arising from dynamical processes in the exoplanet atmosphere. The original HRS detection of CO during the transit of HD 209458 b was accompanied by a 2 ± 1 km/s blue-shift in the planet spectrum in excess of its expected total velocity (based on equation 4). This was interpreted as a fast wind blowing from the highly irradiated dayside of the planet all around the limb to its nightside and was supported by theoretical prediction (Miller-Ricci Kempton and Rauscher 2012; Showman et al. 2013; Kempton et al. 2014). A similarly fast wind was also observed later during the transit of the hot Jupiter HD 189733 b, detected at both optical and infrared wavelengths (Louden and Wheatley 2015; Brogi et al. 2016), via independent analysis techniques. Louden and Wheatley (2015) were able to further demonstrate, by studying the line profile of sodium in the planet's optical transmission spectrum, that the winds on this hot Jupiter form an eastward equatorial jet, with leading and trailing limbs of the planet giving different velocity offsets. Measuring wind speeds may help us understand why hot Jupiters have larger radii than expected, by revealing how they dissipate kinetic energy in the presence of magnetic fields (see e.g. Koll and Komacek 2018, and Laughlin's chapter of this handbook for more discussion on this issue). Simulations also predict that east- or westward hot spots on hot Jupiters could be revealed by velocity excesses when observing the dayside of the planet with HRS (Zhang et al. 2017) and may allow a measurement of the planet's magnetic field strength (Rogers 2017).

A high-resolution future for exoplanet atmospheres

Despite the exciting advances in exoplanet detection and characterization already achieved with high-resolution spectroscopy, the technique is still in its infancy. This is largely due to the scarcity of high-resolution spectrographs, with CRIRES/VLT (8-m) at $R = 100,000$ being the primary resource for the technique between 2010 and 2014, after which CRIRES was removed for upgrades. However, Lockwood et al. (2014) demonstrated that HRS would work at $R = 25,000$ using NIRSPEC/Keck

II (10-m), trading spectral resolution for increased telescope aperture and wider wavelength coverage. The instrument variables of spectral resolution, throughput, aperture size, and instantaneous wavelength coverage can therefore be balanced such that smaller telescopes could be as powerful as the VLT for HRS for the brightest giant exoplanets. Brogi et al. (2018) confirmed this by detecting water vapour in HD 189733 b with GIANO ($R = 50,000$) on the 3.6-m TNG. The upgraded CRIRES+ returns to the VLT in 2019, with a wider instantaneous spectral coverage that will enhance the signal-to-noise of the planet detection via $\sqrt{N_{\text{lines}}}$. Moreover, a large suite of high-resolution spectrographs will soon come online across the globe, driven by the radial velocity hunt for Earth-like planets. This requires very stable, high-resolution spectrographs at optical or infrared wavelengths making them also ideal instruments for HRS of exoplanet atmospheres. Some of the forerunners include the infrared spectrographs: iSHELL/IRTF, CARMENES/CAHA, GIANO/TNG, SPIRou/CFHT, ARIES/MMT, IGRINS/Gemini, HPF/HET, IRD/Subaru, iLocator/LBT, CRIRES+/VLT, and NIRSPEC/Keck, to name but a few, while the optical will see great advances with e.g. ESPRESSO/VLT and EXPRES/DCT (see Wright and Robertson 2017 for a comprehensive list). This suite will enable the study of smaller, cooler planets with HRS than achieved so far. Looking further ahead to the mid-2020s, the first light instruments in the era of the extremely large telescopes (ELTs), also include high-resolution spectrographs e.g. METIS/ELT (Brandl et al. 2014) in the infrared and G-CLEF/GMT (Szentgyorgyi et al. 2016) in the optical. The ELTs will make substantial advances with HRS, including the detection of less abundant chemical species in exoplanet atmospheres. This is important for identifying biomarkers in rocky planet atmospheres, as well as isotopologues that might indicate the evolutionary history of the planet. It will also enable phase-resolved (e.g. dusk/dawn, day/night) studies of exoplanet atmospheres.

One of the most tantalizing prospects for future instrumentation is the detection of an atmosphere surrounding our nearest potentially habitable neighbour, Proxima b (Snellen et al. 2015; Lovis et al. 2017; Wang et al. 2017). The oxygen band at 760nm is an ideal target for HRS+HCI in this non-transiting system. The reflected light from Proxima b will be Doppler-shifted, but it will not contain many photons from the thermal spectrum of the planet. Instead it will be dominated by the stellar spectrum but modulated by the planet's reflection spectrum, adding additional components to the model templates needed when cross-correlating. The development of HRS for detecting and interpreting reflected light from exoplanets is under way (see e.g. Charbonneau et al. 1999; Leigh et al. 2003; Collier-Cameron et al. 2004; Martins et al. 2015; Hoeijmakers et al. 2017). In the exceptional case of a transiting, habitable zone Earth-like planet discovered orbiting a nearby M-dwarf, the oxygen band is again accessible with HRS during the planet's transit. The expected depth of the lines is only $\sim 3\times$ smaller than for CO in a hot Jupiter, but the host star is likely to be very faint and thus requires the photon-collecting power of an ELT (Snellen et al. 2013; Rodler et al. 2013).

Finally, for the widely separated planets, the ELTs may make it possible to map out features such as large storms in their atmospheres, due to the perturbations that

they cause in the spectral line profile. This is similar to how spots are mapped out on stars, or the Rossiter-McLaughlin effect during a planetary transit. It uses Doppler tomography, i.e. it studies how the line profile (or shape of the cross-correlation function) changes as a feature rotates in and out of view. Such a map was recently created for a nearby brown dwarf using the VLT, giving promise to the technique's success to map out the appearance of gas giant exoplanets in the future (Snellen et al. 2014; Crossfield et al. 2014).

Acknowledgements JLB thanks Eleanor Spring, Matteo Brogi, Ignas Snellen, Henriette Schwarz, Jens Hoeijmakers, Ernst de Mooij, and Remco de Kok for helpful discussions on this chapter. This work was performed in part under contract with the Jet Propulsion Laboratory (JPL) funded by NASA through the Sagan Fellowship Program executed by the NASA Exoplanet Science Institute.

References

- Allart R, Lovis C, Pino L et al. (2017) Search for water vapor in the high-resolution transmission spectrum of HD 189733b in the visible. *A&A*606:A144
- Anglada-Escudé G, Amado PJ, Barnes J et al. (2016) A terrestrial planet candidate in a temperate orbit around Proxima Centauri. *Nature*536:437–440
- Baraffe I, Homeier D, Allard F Chabrier G (2015) New evolutionary models for pre-main sequence and main sequence low-mass stars down to the hydrogen-burning limit. *A&A*577:A42
- Barman TS, Konopacky QM, Macintosh B Marois C (2015) Simultaneous Detection of Water, Methane, and Carbon Monoxide in the Atmosphere of Exoplanet HR8799b. *ApJ*804:61
- Barnes JR, Barman TS, Prato L et al. (2007a) Limits on the 2.2- μm contrast ratio of the close-orbiting planet HD 189733b. *MNRAS*382:473–480
- Barnes JR, Leigh CJ, Jones HRA et al. (2007b) Near-infrared spectroscopic search for the close orbiting planet HD 75289b. *MNRAS*379:1097–1107
- Birkby J, Nefs B, Hodgkin S et al. (2012) Discovery and characterization of detached M dwarf eclipsing binaries in the WFCAM Transit Survey. *MNRAS*426:1507–1532
- Birkby JL, de Kok RJ, Brogi M et al. (2013) Detection of water absorption in the day side atmosphere of HD 189733 b using ground-based high-resolution spectroscopy at 3.2 μm . *MNRAS*436:L35–L39
- Birkby JL, de Kok RJ, Brogi M, Schwarz H Snellen IAG (2017) Discovery of Water at High Spectral Resolution in the Atmosphere of 51 Peg b. *AJ*153:138
- Bonfils X, Astudillo-Defru N, Díaz R et al. (2018) A temperate exo-Earth around a quiet M dwarf at 3.4 parsec. *A&A*613:A25
- Brandl BR, Feldt M, Glasse A et al. (2014) METIS: the mid-infrared E-ELT imager and spectrograph. In: *Ground-based and Airborne Instrumentation for Astronomy V*, Proc SPIE, vol 9147, p 914721, DOI 10.1117/12.2056468
- Brogi M, Snellen IAG, de Kok RJ et al. (2012) The signature of orbital motion from the dayside of the planet τ Boötis b. *Nature*486:502–504
- Brogi M, Snellen IAG, de Kok RJ et al. (2013) Detection of Molecular Absorption in the Dayside of Exoplanet 51 Pegasi b? *ApJ*767:27
- Brogi M, de Kok RJ, Birkby JL, Schwarz H Snellen IAG (2014) Carbon monoxide and water vapor in the atmosphere of the non-transiting exoplanet HD 179949 b. *A&A*565:A124
- Brogi M, de Kok RJ, Albrecht S et al. (2016) Rotation and Winds of Exoplanet HD 189733 b Measured with High-dispersion Transmission Spectroscopy. *ApJ*817:106
- Brogi M, Line M, Bean J, Désert JM Schwarz H (2017) A Framework to Combine Low- and High-resolution Spectroscopy for the Atmospheres of Transiting Exoplanets. *ApJ*839:L2

- Brogi M, Jacobbe P, Guilluy G et al. (2018) Exoplanet atmospheres with GIANO. I. Water in the transmission spectrum of HD 189733b. ArXiv e-prints
- Brown TM (2001) Transmission Spectra as Diagnostics of Extrasolar Giant Planet Atmospheres. *ApJ*553:1006–1026
- Brown TM, Libbrecht KG Charbonneau D (2002) A Search for CO Absorption in the Transmission Spectrum of HD 209458b. *PASP*114:826–832
- Charbonneau D, Jha S Noyes RW (1998) Spectral Line Distortions in the Presence of a Close-in Planet. *ApJ*507:L153–L156
- Charbonneau D, Noyes RW, Korzennik SG et al. (1999) An Upper Limit on the Reflected Light from the Planet Orbiting the Star τ Bootis. *ApJ*522:L145–L148
- Collier Cameron A, Horne K, Penny A James D (1999) Probable detection of starlight reflected from the giant planet orbiting τ Boötis. *Nature*402:751–755
- Collier-Cameron A, Horne K, James D, Penny A Semel M (2004) τ Boo b: Not so bright, but just as heavy. In: Penny A (ed) Planetary Systems in the Universe, IAU Symposium, vol 202, p 75
- Crossfield IJM Kreidberg L (2017) Trends in Atmospheric Properties of Neptune-size Exoplanets. *AJ*154:261
- Crossfield IJM, Barman T Hansen BMS (2011) High-resolution, Differential, Near-infrared Transmission Spectroscopy of GJ 1214b. *ApJ*736:132
- Crossfield IJM, Biller B, Schlieder JE et al. (2014) A global cloud map of the nearest known brown dwarf. *Nature*505:654–656
- de Kok RJ, Brogi M, Snellen IAG et al. (2013) Detection of carbon monoxide in the high-resolution day-side spectrum of the exoplanet HD 189733b. *A&A*554:A82
- de Kok RJ, Birkby J, Brogi M et al. (2014) Identifying new opportunities for exoplanet characterisation at high spectral resolution. *A&A*561:A150
- Deming D, Seager S, Richardson LJ Harrington J (2005) Infrared radiation from an extrasolar planet. *Nature*434:740–743
- Dittmann JA, Irwin JM, Charbonneau D et al. (2017) Discovery and Precise Characterization by the M-Planet Project of LP 661-13, an Eclipsing Binary Consisting of Two Fully Convective Low-mass Stars. *ApJ*836:124
- Dressing CD Charbonneau D (2015) The Occurrence of Potentially Habitable Planets Orbiting M Dwarfs Estimated from the Full Kepler Dataset and an Empirical Measurement of the Detection Sensitivity. *ApJ*807:45
- Esteves LJ, de Mooij EJW, Jayawardhana R, Watson C de Kok R (2017) A Search for Water in a Super-Earth Atmosphere: High-resolution Optical Spectroscopy of 55Cnc e. *AJ*153:268
- Fulton BJ, Petigura EA, Howard AW et al. (2017) The California-Kepler Survey. III. A Gap in the Radius Distribution of Small Planets. *AJ*154:109
- Gillon M, Triaud AHMJ, Demory BO et al. (2017) Seven temperate terrestrial planets around the nearby ultracool dwarf star TRAPPIST-1. *Nature*542:456–460
- Gordon I, Rothman L, Hill C et al. (2017) The hitran2016 molecular spectroscopic database. *Journal of Quantitative Spectroscopy and Radiative Transfer* 203:3 – 69, URL <http://www.sciencedirect.com/science/article/pii/S0022407317301073>, HITRAN2016 Special Issue
- Hargreaves RJ, Bernath PF, Bailey J Dulick M (2015) Empirical Line Lists and Absorption Cross Sections for Methane at High Temperatures. *ApJ*813:12
- Heng K (2016) A Cloudiness Index for Transiting Exoplanets Based on the Sodium and Potassium Lines: Tentative Evidence for Hotter Atmospheres Being Less Cloudy at Visible Wavelengths. *ApJ*826:L16
- Henry TJ, Ianna PA, Kirkpatrick JD Jahreiss H (1997) The solar neighborhood IV: discovery of the twentieth nearest star. *AJ*114:388–395
- Henry TJ, Jao WC, Winters JG et al. (2016) The Census of Objects within 10 Parsecs. In: American Astronomical Society Meeting Abstracts, American Astronomical Society Meeting Abstracts, vol 227, p 142.01
- Henry TJ, Jao WC, Winters JG et al. (2018) The Solar Neighborhood XLIV: RECONS Discoveries within 10 Parsecs. ArXiv e-prints

- Hoeijmakers HJ, de Kok RJ, Snellen IAG et al. (2015) A search for TiO in the optical high-resolution transmission spectrum of HD 209458b: Hindrance due to inaccuracies in the line database. *A&A*575:A20
- Hoeijmakers HJ, Snellen IAG van Terwisga SE (2017) Searching for reflected light from τ Bootis b with high-resolution ground-based spectroscopy: Approaching the 10^{-5} contrast barrier. ArXiv e-prints
- Hoeijmakers HJ, Schwarz H, Snellen IAG et al. (2018) Medium-resolution integral-field spectroscopy for high-contrast exoplanet imaging: Molecule maps of the β Pictoris system with SINFONI. ArXiv e-prints
- Hörst SM, He C, Lewis NK et al. (2018) Haze production rates in super-Earth and mini-Neptune atmosphere experiments. *Nature Astronomy* 2:303–306
- Irwin JM, Quinn SN, Berta ZK et al. (2011) LSPM J1112+7626: Detection of a 41 Day M-dwarf Eclipsing Binary from the MEarth Transit Survey. *ApJ*742:123
- Jackson RJ, Deliyannis CP, Jeffries RD (2018) The inflated radii of M dwarfs in the Pleiades. *MNRAS*476:3245–3262
- Kalman D (1996) A singularly valuable decomposition: The svd of a matrix. *The College Mathematics Journal* 27(1):2–23, URL <http://www.jstor.org/stable/2687269>
- Kempton EMR, Perna R, Heng K (2014) High Resolution Transmission Spectroscopy as a Diagnostic for Jovian Exoplanet Atmospheres: Constraints from Theoretical Models. *ApJ*795:24
- Kesseli AY, Muirhead PS, Mann AW, Mace G (2018) Magnetic Inflation and Stellar Mass. II. On the Radii of Single, Rapidly Rotating, Fully Convective M-Dwarf Stars. *AJ*155:225
- Koll DDB, Komacek TD (2018) Atmospheric Circulations of Hot Jupiters as Planetary Heat Engines. *ApJ*853:133
- Konopacky QM, Barman TS, Macintosh BA, Marois C (2013) Detection of Carbon Monoxide and Water Absorption Lines in an Exoplanet Atmosphere. *Science* 339:1398–1401
- Kreidberg L, Bean JL, Désert JM et al. (2014a) Clouds in the atmosphere of the super-Earth exoplanet GJ1214b. *Nature*505:69–72
- Kreidberg L, Bean JL, Désert JM et al. (2014b) A Precise Water Abundance Measurement for the Hot Jupiter WASP-43b. *ApJ*793:L27
- Leigh C, Collier Cameron A, Udry S et al. (2003) A search for starlight reflected from HD 75289b. *MNRAS*346:L16–L20
- Lockwood AC, Johnson JA, Bender CF et al. (2014) Near-IR Direct Detection of Water Vapor in Tau Boötis b. *ApJ*783:L29
- López-Morales M, Ribas I (2005) GU Bootis: A New $0.6M_{\text{solar}}$ Detached Eclipsing Binary. *ApJ*631:1120–1133
- Louden T, Wheatley PJ (2015) Spatially Resolved Eastward Winds and Rotation of HD 189733b. *ApJ*814:L24
- Lovis C, Fischer D (2010) *Radial Velocity Techniques for Exoplanets*, University of Arizona Press, pp 27–53
- Lovis C, Snellen I, Mouillet D et al. (2017) Atmospheric characterization of Proxima b by coupling the SPHERE high-contrast imager to the ESPRESSO spectrograph. *A&A*599:A16
- Lubin JB, Rodriguez JE, Zhou G et al. (2017) A Bright Short Period M-M Eclipsing Binary from the KELT Survey: Magnetic Activity and the Mass-Radius Relationship for M Dwarfs. *ApJ*844:134
- Macintosh B, Graham JR, Barman T et al. (2015) Discovery and spectroscopy of the young jovian planet 51 Eri b with the Gemini Planet Imager. *Science* 350:64–67
- Martins JHC, Santos NC, Figueira P et al. (2015) Evidence for a spectroscopic direct detection of reflected light from ι ASTROBJ $_{\zeta}$ 51 Pegasi b $_{\zeta}$ /ASTROBJ $_{\zeta}$. *A&A*576:A134
- Mayor M, Queloz D (1995) A Jupiter-mass companion to a solar-type star. *Nature*378:355–359
- Miller-Ricci Kempton E, Rauscher E (2012) Constraining High-speed Winds in Exoplanet Atmospheres through Observations of Anomalous Doppler Shifts during Transit. *ApJ*751:117
- Murtagh F, Heck A (eds) (1987) *Multivariate Data Analysis, Astrophysics and Space Science Library*, vol 131, DOI 10.1007/978-94-009-3789-5

- Nugroho SK, Kawahara H, Masuda K et al. (2017) High-resolution Spectroscopic Detection of TiO and a Stratosphere in the Day-side of WASP-33b. *AJ*154:221
- Parmetier V, Line MR, Bean JL et al. (2018) From thermal dissociation to condensation in the atmospheres of ultra hot Jupiters: WASP-121b in context. ArXiv e-prints
- Pino L, Ehrenreich D, Wyttenbach A et al. (2018) Combining low- to high-resolution transit spectroscopy of HD 189733b. Linking the troposphere and the thermosphere of a hot gas giant. *A&A*612:A53
- Piskorz D, Benneke B, Crockett NR et al. (2016) Evidence for the Direct Detection of the Thermal Spectrum of the Non-Transiting Hot Gas Giant HD 88133 b. *ApJ*832:131
- Piskorz D, Benneke B, Crockett NR et al. (2017) Detection of Water Vapor in the Thermal Spectrum of the Non-transiting Hot Jupiter Upsilon Andromedae b. *AJ*154:78
- Press WH, Teukolsky SA, Vetterling WT Flannery BP (1992) Numerical recipes in FORTRAN. The art of scientific computing. Cambridge: University Press, —c1992, 2nd ed.
- Rodler F, Lopez-Morales M Ribas I (2012) Weighing the Non-transiting Hot Jupiter τ Boo b. *ApJ*753:L25
- Rodler F, Kürster M Barnes JR (2013) Detection of CO absorption in the atmosphere of the hot Jupiter HD 189733b. *MNRAS*432:1980–1988
- Rogers TM (2017) Constraints on the magnetic field strength of HAT-P-7 b and other hot giant exoplanets. *Nature Astronomy* 1:0131
- Rothman L, Gordon I, Babikov Y et al. (2013) The hitran2012 molecular spectroscopic database. *Journal of Quantitative Spectroscopy and Radiative Transfer* 130:4 – 50, URL <http://www.sciencedirect.com/science/article/pii/S0022407313002859>, hITRAN2012 special issue
- Rothman LS, Gordon IE, Barber RJ et al. (2010) HITEMP, the high-temperature molecular spectroscopic database. *J Quant Spectr Rad Transf*111:2139–2150
- Schwarz H, Brogi M, de Kok R, Birkby J Snellen I (2015) Evidence against a strong thermal inversion in HD 209458b from high-dispersion spectroscopy. *A&A*576:A111
- Schwarz H, Ginski C, de Kok RJ et al. (2016) The slow spin of the young substellar companion GQ Lupi b and its orbital configuration. *A&A*593:A74
- Showman AP, Fortney JJ, Lewis NK Shabram M (2013) Doppler Signatures of the Atmospheric Circulation on Hot Jupiters. *ApJ*762:24
- Sing DK, Fortney JJ, Nikolov N et al. (2016) A continuum from clear to cloudy hot-Jupiter exoplanets without primordial water depletion. *Nature*529:59–62
- Smette A, Sana H, Noll S et al. (2015) Molecfit: A general tool for telluric absorption correction. I. Method and application to ESO instruments. *A&A*576:A77
- Snellen I, de Kok R, Birkby JL et al. (2015) Combining high-dispersion spectroscopy with high contrast imaging: Probing rocky planets around our nearest neighbors. *A&A*576:A59
- Snellen IAG, de Kok RJ, de Mooij EJW Albrecht S (2010) The orbital motion, absolute mass and high-altitude winds of exoplanet HD209458b. *Nature*465:1049–1051
- Snellen IAG, de Kok RJ, le Poole R, Brogi M Birkby J (2013) Finding Extraterrestrial Life Using Ground-based High-dispersion Spectroscopy. *ApJ*764:182
- Snellen IAG, Brandl BR, de Kok RJ et al. (2014) Fast spin of the young extrasolar planet β Pictoris b. *Nature*509:63–65
- Sparks WB Ford HC (2002) Imaging Spectroscopy for Extrasolar Planet Detection. *ApJ*578:543–564
- Szentgyorgyi A, Baldwin D, Barnes S et al. (2016) The GMT-Consortium Large Earth Finder (G-CLEF): an optical Echelle spectrograph for the Giant Magellan Telescope (GMT). In: Ground-based and Airborne Instrumentation for Astronomy VI, Proc SPIE, vol 9908, p 990822, DOI 10.1117/12.2233506
- Tamuz O, Mazeh T Zucker S (2005) Correcting systematic effects in a large set of photometric light curves. *MNRAS*356:1466–1470
- Tennyson J, Yurchenko SN, Al-Refaie AF et al. (2016) The ExoMol database: Molecular line lists for exoplanet and other hot atmospheres. *Journal of Molecular Spectroscopy* 327:73–94

- Torres G, Andersen J Giménez A (2010) Accurate masses and radii of normal stars: modern results and applications. *A&A Rev*18:67–126
- Van Eylen V, Agentoft C, Lundkvist MS et al. (2017) An asteroseismic view of the radius valley: stripped cores, not born rocky. *ArXiv e-prints*
- Walker GAH, Matthews JM, Kuschnig R et al. (2006) Precise photometry of 51 Peg systems with MOST. In: Arnold L, Bouchy F Moutou C (eds) Tenth Anniversary of 51 Peg-b: Status of and prospects for hot Jupiter studies, pp 267–273
- Wang J, Mawet D, Ruane G, Hu R Benneke B (2017) Observing Exoplanets with High Dispersion Coronagraphy. I. The Scientific Potential of Current and Next-generation Large Ground and Space Telescopes. *AJ*153:183
- Welch BL (1947) The generalization of ‘student’s’ problem when several different population variances are involved. *Biometrika* 34(1/2):28–35, URL <http://www.jstor.org/stable/2332510>
- Wiedemann G (1996) Science with the VLT: high-resolution infrared spectroscopy. *The Messenger* 86:24–30
- Wiedemann G (2000) Direct spectroscopic detection and characterization of short-period extra-solar planets. In: Bergeron J (ed) Discoveries and Research Prospects from 8- to 10-Meter-Class Telescopes, *Proc SPIE*, vol 4005, pp 260–262, DOI 10.1117/12.390150
- Wright JT Robertson P (2017) The Third Workshop on Extremely Precise Radial Velocities: The New Instruments. *Research Notes of the American Astronomical Society* 1(1):51
- Zhang J, Kempton EMR Rauscher E (2017) Constraining Hot Jupiter Atmospheric Structure and Dynamics through Doppler-shifted Emission Spectra. *ApJ*851:84
- Zucker S Mazeh T (1994) Study of spectroscopic binaries with TODCOR. 1: A new two-dimensional correlation algorithm to derive the radial velocities of the two components. *ApJ*420:806–810